Proceedings of Global Power and Propulsion Society
ISSN-Nr: 2504-4400
GPPS Hong Kong 2023
October 17-19, 2023
www.gpps.global

GPPS-TC-2023-0090

EFFECTS OF INLET DISTORTION ON AEROELASTIC STABILITY OF A TRANSONIC FAN

Yun Zheng
School of Energy and Power Engineering
Beihang University
zheng_yun@buaa.edu.cn
Beijing, China

Penghui Guo
School of Energy and Power Engineering
Beihang University
ZY2104504@buaa.edu.cn
Beijing, China

Hui Yang
School of Energy and Power Engineering
Beihang University
huiyang@buaa.edu.cn
Beijing, China

Kang Xu
35th Inst.
CASIC
xukang@buaa.edu.cn
Beijing, China

ABSTRACT

The BLI-type engine makes fan blades work in the state of inlet distortion. The effects of this kind of distortion on the aeromechanical characteristics of fan blades are studied numerically. An in-house coupled fluid/structure numerical code is used for the prediction of the vibration response of rotor blades. The three-dimensional, time-accurate, unsteady Reynolds-Averaged Navier-Stokes (RANS) equations are solved in the fluid domain, and the structural dynamic equations of blade vibration are solved with a modal superimposition method. Aeromechanical response of the transonic fan—NASA rotor67 with inlet total pressure distortion is studied in detail. Full-annulus aeroelastic calculations under both clean and distorted(DC180) flow conditions are conducted, and the overall aerodynamic damping of the rotor is shown.

Compared with the case in clean flow, the aerodynamic damping with inlet distortion is reduced. The effects of the distortion coefficient describing the intensity of inlet distortion on fan aeromechanical characteristics are also investigated. Results show that an inlet distortion with higher intensity(distortion coefficient=0.9 (DIS-0.9)) will increase the risk of flutter occurrence.

Keywords inlet distortion; shock wave; aerodynamic damping; flutter

INTRODUCTION

Inlet distortion is a well-known and inevitable problem in aircraft engines. Rapid climbing can cause total pressure and swirl distortion. Civil aircraft engines may also experience non-uniform inflow due to ground vortex and Boundary Layer Ingestion (BLI). With the improvement of the engine performance and the wide use of lightweight materials, fan blades must withstand harsh unsteady loadings from distorted flows, which can push them to their limits of material strength and fatigue. Thus, mechanical integrity must be ensured in the design process to prevent High Cycle Fatigue (HCF) caused by flutter.

Previous studies mainly focused on the influence of inlet distortion on aerodynamic characteristics, such as the degradation of performance and stability margin. Pearson and McKenzie (1959) proposed a parallel compressor model for distortion analysis, and Reid (1969) developed the concept of the critical angle of spoiling, as the spoiled angle was increased from 0 to 90 deg, the surge delivery static pressure fell rapidly and then stabilized at a constant minimum value from 90 to 360 deg. Subsequently, Greitzer (1976), Roberts (1968), Adamczyk (1974), Mazzawy (1977), and Lecht (1983) improved and optimized the parallel compressor model. Moreover, actuator discs and semi-actuator discs (Hsuan Yeh, 1959) were introduced in the evaluation of inlet distortion. With the improvement of Computational Fluid Dynamics (CFD), some high-fidelity numerical methods (Yao J et al, 2010) were also applied to the study of distortion.

In addition, non-uniform inflow conditions could also result in aeromechanical issues, such as distortion effects on

flutter boundaries. Danforth (1975) summarized eight types of blade vibration caused by several inlet distortions, and a distortion coefficient based on energy transfer was introduced.

The effects of inlet distortion on flutter stability cannot be ignored. Halliwell (1980) studied the effects of varying engine intake conditions on the supersonic flutter of turbofan engines and a tentative relationship was derived between this distortion and flutter onset speed. Herrick (2010, 2014) studied forward-swept high-speed fan flutter stability in the presence of sinusoidal distortion of total pressure through both one-way and two-way coupled methods. The research found that the fan in distorted flow was slightly less stable than in clean flow, and there existed great variations in aerodynamic work from blade to blade caused by distortion. More recent studies on the aeromechanical characteristics of a distortion-tolerant fan with BLI were conducted by Provenza (2018), Duffy (2018), and Bakhle (2018). In their research, high-fidelity computational code and wind tunnel test were used to study the aeromechanical characteristics of a fan in both uniform and distorted flow, and results showed that the fan remained flutter-free except at one near-stall operating condition.

Compared with large numbers of studies on fan performance and stability due to inlet distortion, papers focusing on the aeromechanical characteristics are far from enough. In particular, previous studies of the effects of inlet distortion on flutter have not yet come to a unified conclusion, and the mechanism for this is not clear.

In this paper, a time-accurate fluid-structure coupled aeroelastic method is applied in the prediction of the fan blade vibratory response. NASA rotor67 with inlet circumferential total pressure distortion is studied at 100% rotational speed near the stall. Unsteady loadings, blade displacements, and aerodynamic damping are presented with both clean and distorted flow. The aeromechanical characteristics with different distortion coefficients are analyzed in detail.

NUMERICAL METHODOLOGY

The CFD code used in this study is HGAE (Hybrid Grid Aeroelasticity Environment), a three-dimensional, unsteady, time-accurate, Reynolds-Averaged Navier-Stokes solver for turbomachinery applications. More details can be found in Zheng Yun (2011). The CFD code has been validated in various aerodynamic and aeroelastic cases (Zheng Y et al, 2009; 2011; 2013)

Aerodynamic Models

Due to the time-varying movement and deformation of the fluid domain grid in most fluid-structure coupling models, the governing equations for fluid motion should be solved in Arbitrary-Lagrangian Eulerian (ALE) reference frame. The unsteady compressible Navier-Stokes equations are expressed as a system of conservation laws of mass, momentum, and energy in the control volume. The integral form of these equations in the ALE reference frame is given as:

$$\frac{\partial}{\partial t}\int_{\Omega}\vec{q}\,d\Omega + \oint_{\partial\Omega}\left(\overrightarrow{F_c} - \overrightarrow{F_v}\right)dS = \int_{\Omega}\vec{S}\,d\Omega \tag{1}$$

where $\vec{q}$ is the conservative variable vector. Ω is the control volume and $\partial\Omega$ is the boundary. $\overrightarrow{F_c}$ and $\overrightarrow{F_v}$ represent the convective and viscous fluxes, and $\vec{S}$ is the source term vector.

The turbulence model adopted in this paper is the one-equation Spalart-Allmaras model. The S-A model is one of the most widely used turbulence models in turbomachinery applications. This model was developed by summarizing the experimental results of the typical boundary layer flow. It has the advantages of simple form, good convergence, and high accuracy in most applications.

The governing equations are discretized with a second-order accurate Monotone Upstream-centered Scheme for Conservation Laws (MUSCL) scheme with a VanLeer limiter, based on a Finite Volume Method (FVM) for multi-block structured grids. Roe Flux Difference Splitting (FDS) upstream scheme is employed for fluxes evaluation because of accuracy and efficiency. The flow solver uses a second-order accurate implicit temporal discretization. A dual time stepping procedure with 12 sub-iterations is employed for unsteady flow computations.

Structural Model

In most flutter problems, the structure vibration is modeled by a linear model. The structural dynamic equation for the blade vibration is given as:

$$M\ddot{x} + C\dot{x} + Kx = Q \tag{2}$$

where *M*, *C,* and *K* represent the mass, damping, and stiffness matrices respectively. *x* and *Q* are the displacement and aerodynamic force vectors. The deflection of blade vibration can be expressed as a linear combination of mode shapes, such as:

$$\mathrm{x}=\phi\mathrm{q} \tag{3}$$

where q is the generalized coordinate vector. ϕ is the mass-averaged mode shape matrix. Then Eq. (3) can be decoupled into a system of *N* linearly independent ordinary differential equations, as:

$$M_g\ddot{q} + C_g\dot{q} + K_g q = Q_g \tag{4}$$

where q, $\dot{q}$, and $\ddot{q}$ represent the modal displacement, modal velocity, and modal acceleration vectors. M_g, C_g, and K_g can be derived from the mass normalization of the mass, damping, and stiffness matrices. Q_g is the generalized aerodynamic force vector.

Fluid-structure Coupling

An integrated aeroelasticity numerical method is used in fluid-structure coupling problems. It solves the aerodynamic equations and the structural dynamic equations simultaneously, and the boundary conditions from the aerodynamic and structural domains are exchanged at each time step. The aerodynamic force vector is solved from Eq. (1) and serves as the right-hand side of Eq. (2). Then the displacement of each point on the blade surface is computed. Next, a grid deformation technique is used to update the new blade position. Convergence is achieved by performing the above computational cycle.

DISTORTION PATTERN

To avoid potential interference of the fan on upstream distortion and ensure that the flow field at the fan outlet can fully develop, the inlet boundary is set at one rotor diameter upstream of the rotor blade leading edge, and the exit boundary is set at a distance of 1.5 diameters downstream of the rotor trailing edge(Figure 1).

The inlet distortion is processed as inflow boundary conditions, given by the total pressure. High and low-pressure regions account for half of the total area (Figure 1). Figure 2 shows that the circumferential distribution of total pressure appears as a square wave.

Three different distortion coefficients are studied in this paper. Detailed information is in Table 1.

Table 1. Distortion Type

Type	P^*_{MIN}/P^*_{MAX}	P^*_{AVG}(Pa)
CLEAN	1.00	101325
DIS-0.95	0.95	101325
DIS-0.90	0.90	101325

The value of total pressure is constant along the radial direction, and varies along the circumferential direction. The circumferential distribution of total pressure is a square wave as shown in Figure 2. The Fourier series expansion of the square wave is based on:

$$P^*(\theta)=P_0^*+\frac{4P^*_{amp}}{\pi}\sum_{i=1}^{\infty}\frac{\sin(\omega_i\theta)}{2n-1},\omega_i=(2n-1)\frac{2\pi}{T},n=1,2,3\ldots \quad (5)$$

where $P^*(\theta)$ is the total pressure as a function of circumferential location — θ. P_0^* and P^*_{amp} are the mean value and the amplitude respectively. The square wave consists of odd-order harmonics without any even-order components as shown in Figure 3.The choice of the 180 degree distortion pattern is due to the simple nature of the model. More typical patterns in practical applications will be studied in the future.

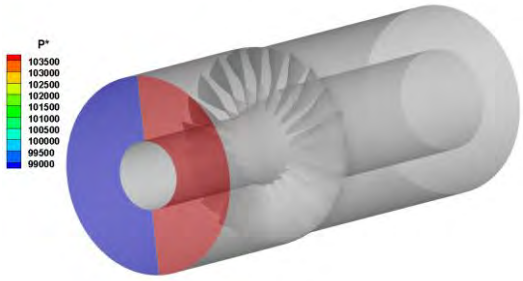

Figure 1: Computational Domain and Distortion Pattern

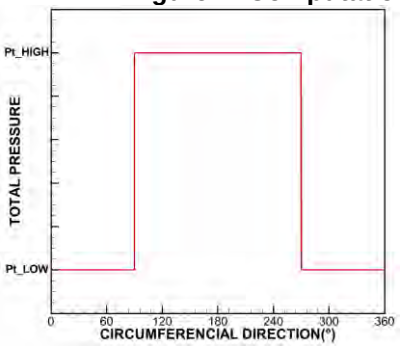

Figure 2: Circumferential Distribution of Total Pressure

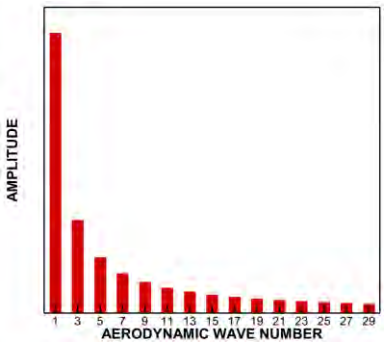

Figure 3: Amplitude Frequency Spectrum of Distortion Pattern

CASE STUDY

The numerical study is based on the low-aspect-ratio transonic axial-flow fan rotor—NASA Rotor67, designed by NASA Lewis Research Center. The fan has 22 blades and an aspect ratio of 1.56, without inlet guide vanes or stators. The

design rotational speed is 16043 rpm. The rotor design pressure ratio is 1.63 at a mass flow of 33.25 kg/sec(Strazisar A J, et al, 1989). More details can be found in Table 2.

Table 2. Fan Design Parameters

Rotational Speed	16043 rpm	Tip Mach	1.38
Flow Rate	33.25 kg/s	Axial Mach	0.49
Pressure Ratio	1.63	Efficiency	0.93
Tip Clearance	1.016 mm	Hub/Tip Ratio	0.375
Number of Blades	22	Aspect Ratio	1.56

Computational Grids

The structured grid with a topology of O4H is shown in Figure 4. The thickness of the first near-wall cell is 1e-5 and y+ is less than 10. There are 61 grid lines from hub to casing, with 17 of them in the tip clearance region. The number of nodes in single-passage is nearly 800,000. Figures 4(a) and (b) show the grid for single-passage and full-annulus, and Figure 4(c) illustrates the grid in the blade-to-blade surface.

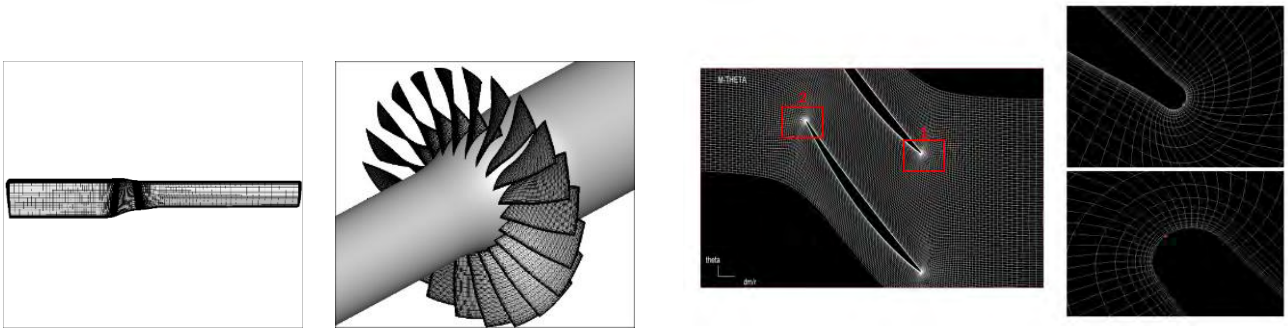

(a) Single-Passage **(b) Full-Annulus** **(c) Blade-to-Blade Surface**

Figure 4: Computational Grids

Results

Fan Performance Analysis

As shown in Figure 5, steady computations are carried out to predict the fan performance at 100% speed. The CFD prediction for uniform inlet condition shows good agreement with the measured result, except for a slight underprediction (2%) of the total pressure ratio. The computed mass flow at chocking point is 34.50 kg/s, and the peak efficiency of 90.3% is obtained at 33.54 kg/s. The point near the stall (labeled as "A") is chosen for the following aeromechanical study. Unsteady computations with different distortion coefficients (CLEAN, DIS-0.95, and DIS-0.90) are carried out to estimate the influence of distortion on fan performance. According to the map, as the intensity of distortion increases, point "A" is closer to the stall margin.

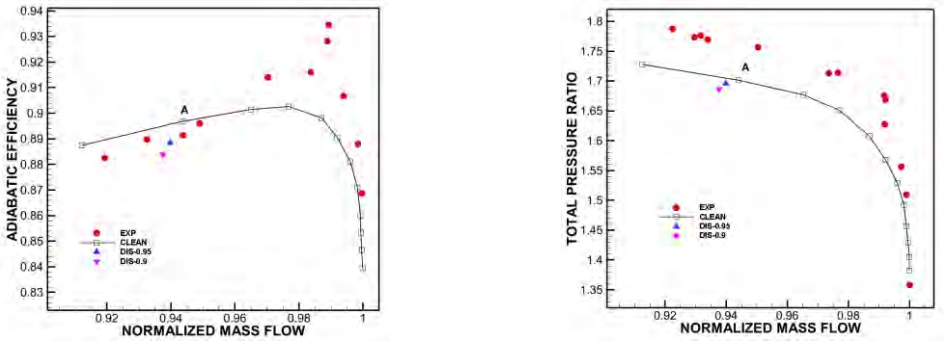

(a) Adiabatic Efficiency **(b) Total Pressure Ratio**

Figure 5: Performance Map of NASA Rotor67

Flutter Analysis

The operation point near-stall is selected for the coupled fluid-structure flutter analysis in the case of clean、dis-0.95 and dis-0.90. The full annulus calculation is started from a converged steady flow solution. An impulse is given to the blade by applying a small initial velocity, and the time history of the modal displacement is recorded for stability analysis.

The pressure contours of blade-to-blade surface at 90% span under the two distortion conditions are shown in Figure 6. Due to the effect of inlet distortion, there are obvious circumferential differences, especially at the two intersections of high and low pressures. In case "dis-0.9", the locally enlarged contours shows that the flow field in the blade tip region presents a shock wave structure. The normal shock wave of the passage presents a bow at the distorted junction of high

and low pressure, which leads to the advance of the intersection point between the shock wave and the blade pressure side. Therefore, a high-pressure airflow mass is formed behind the passage.

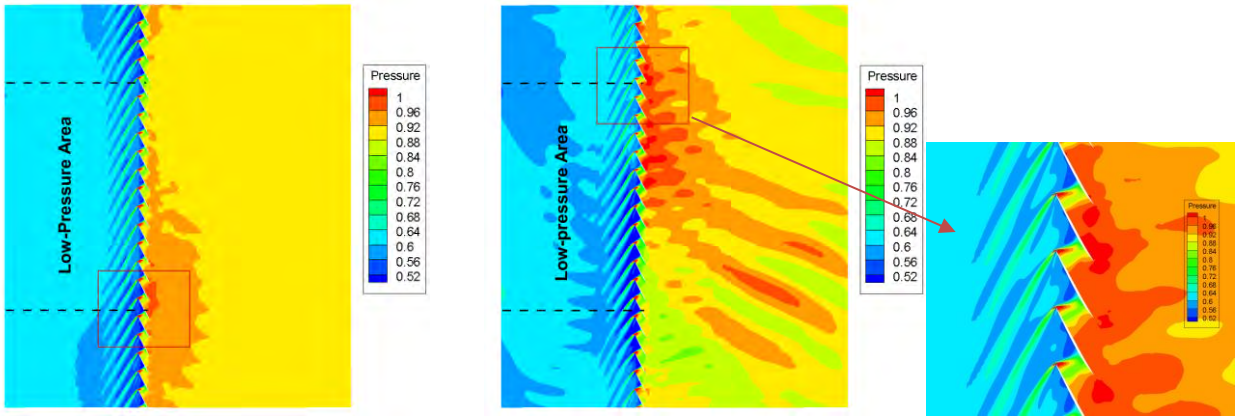

(A) DIS-0.95 **(B) DIS-0.9**

Figure 6: Circumferential contour of the pressure, 90% rotor span

To gain further insight into the flow field and the unsteady pressure, the flow field along the blade surface at 90 percent of the span from the hub is investigated in more detail. The unsteady pressure(non-dimensionalized) of 1 rotational cycle is plotted in Figure 7. In the case of "DIS-0.95", the pressure temporal and spatial distribution diagram shows that the inlet distortion causes oscillations of shock wave around 55% chord without apparent regularity. The significant fluctuation of unsteady pressure indicates an increase in the unsteadiness of the flow field. In the case of "DIS-0.9", the pressure temporal and spatial distribution diagram shows that the chord oscillation of the shock wave is enhanced, and there is an obvious time periodicity. When the blade passes through the low-pressure region, the shock wave is pushed forward and moves backward in the high-pressure region. The process of shock wave movement can be observed in the temporal and spatial distribution diagram of unsteady pressure. Unsteady pressure on the pressure surface has two amplitude fluctuations at the junction of high and low pressure represented by the dotted line. The reason is that the aerodynamic condition changes the most when the blade passes over the junction of high and low pressure, and the shock wave on the suction surface violently oscillates and affects the pressure surface. With the increase of inlet distortion intensity, the non-uniformity of the blade surface flow field is enhanced, and the stability of the flow field becomes worse.

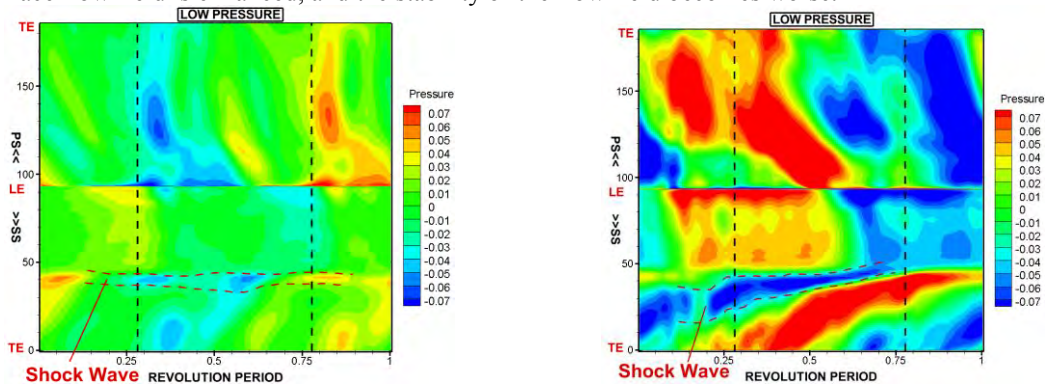

(a) DIS-0.95 **(b) DIS-0.90**

Figure 7: Contour Maps of Temporal and Spatial Distribution of Unsteady Pressure

Due to the concept of cyclic symmetry, the mode shape of a single blade is expanded to obtain the entire rotor assembly mode. The disk is assumed to be rigid. The IBPA (Inter-Blade Phase Angle) is different between adjacent blades in different NDs (Nodal Diameter). There are 22 different NDs in the assembly, referred to as nth ND (forward traveling wave) and −nth ND (backward traveling wave). All 22 NDs are calculated in each case. Figure 8 shows the time histories of modal displacements for the first 4 NDs, as well as Figure 9(a) shows the FFT amplitude spectra of them. It is known that the growing amplitude indicates instability, while the decaying amplitude indicates stability. These are not typical time histories of flutter, because a beating component is included. The FFT amplitude spectra show that nth ND has a beating component of nEO (engine order), and this component is especially significant in odd-order cases. The connection between the beating components and the inlet distortion pattern is obvious. It should be noted that, the inlet distortion type mentioned above consists of no even-order harmonic components, and with the increase of the distortion coefficient, the amplitude of the 2EO beating component increases significantly under the DIS-0.9 condition. The effect of this phenomenon on aeroelastic stability will be analyzed below.

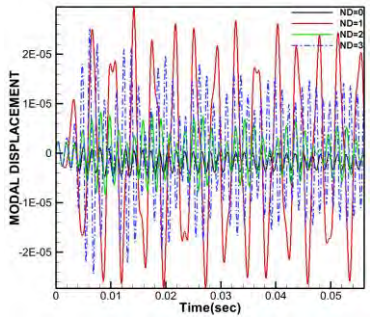

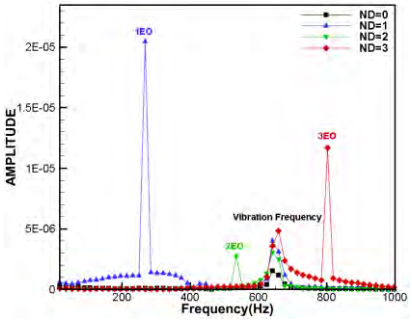

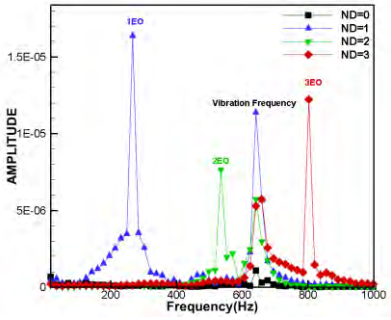

Figure 8: Time Histories of Modal Displacement (DIS-0.95)

(a) DIS-0.95 (b) DIS-0.90

Figure 9: Amplitude Spectra of Different Nodal Diameters

It is hard to calculate the aerodynamic damping with the beating component, so the specific beating components in different NDs are eliminated by wave filtering. Figure 10 shows the time histories of processed modal displacements. The aerodynamic damping is based on the logarithmic decrement of the vibration history, as follows:

$$\delta = \ln \frac{x_t}{x_{t+T}} \quad (6)$$

Where δ is the damping, it is the model displacement at time t and T is the vibration period.

The aeroelastic stability is positively related to the damping, and negative damping is representative of the occurrence of flutter. Figure 11 illustrates that under clean inlet conditions, the aerodynamic damping of the 1st bending mode changes significantly with different nodal diameters, showing an approximately sinusoidal distribution.

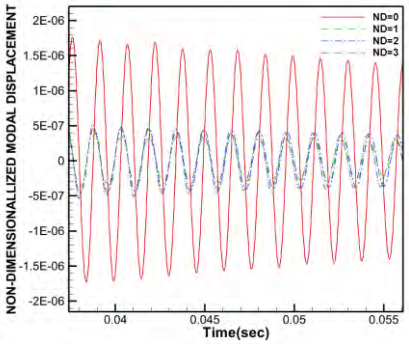

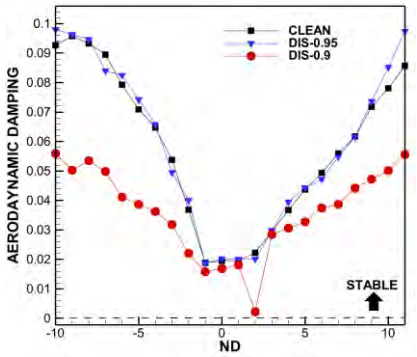

Figure 10: Time Histories of Modal Displacements with Beating Excluded (DIS-0.95)

Figure 11: Aerodynamic Damping

As for the effect of distortion intensity on flutter stability, "DIS-0.95" has almost no change to the aerodynamic damping. However, the flutter stability is significantly reduced when the distortion intensity increases (DIS-0.90). The aerodynamic damping value of 2ND decreases the most. It is mentioned that the amplitude of the 2EO beating component increases significantly at "DIS-0.9", and the circumferential distribution of the exciting force of 2EO is consistent with the assembled mode shape of 2ND.This will promote the modal vibration of 2ND.

To further analyze the impact of inlet distortion on aeroelastic stability, an instantaneous snapshot of the blade surface is analyzed. The streamlines near the blade surface on the suction side (middle of the high-pressure area) are plotted in Figure 12 to show the radial migration of flow, and the separation point is defined as the location where axial flow on the suction side passes the tip clearance (marked in the red cycle).

The axial locations of the separation points on the blade tip in the three cases are plotted in Figure 13. It is obvious that the moving range of the separation point increases with growing distortion intensity, and the size of the separation region on the suction side is dependent on the movement of the shock wave. The moving range of the separation point increases with growing distortion intensity, and the size of the separation region on the suction side is dependent on the movement of the shock wave. In terms of "DIS-0.9", as shown in Figure 3, the position of the shock wave changes drastically when the blade moves in and out of the low-pressure area. The oscillation form of the shock wave is similar to a sine function in one revolution period, which indicates an obvious 2EO excitation to the blade as described in Ref(Pan T 2023). The spatial movement of shock position indicates that the fan rotor becomes less aeroelastic stable with a larger distorted inflow.

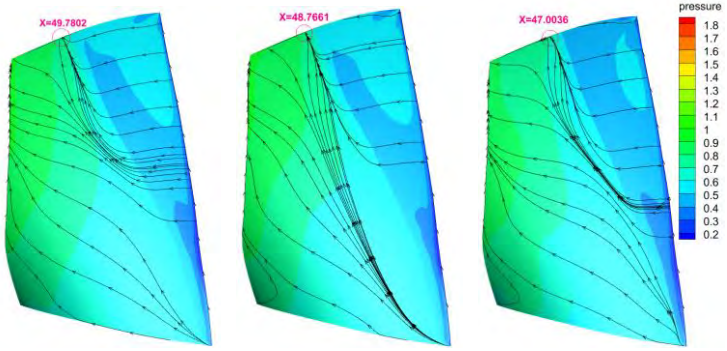

(a) Clean (b) DIS-0.95 (c) DIS-0.9

Figure 12: Streamlines Near the Blade Surface on Suction Side in Three Cases

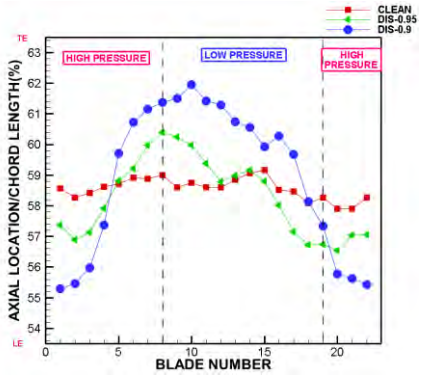

Figure 13: Axial Location of Separation Point on Blade Tip in Three Cases

Under vibration frequency, unsteady pressure on the blade surface was transformed by FFT to obtain the unsteady pressure amplitude distribution on the blade suction surface, as shown in Figure 14. Compared with the two distortion conditions and one clean condition at the same scale, there is an obvious red high amplitude region on the blade suction surface at DIS-0.9, which represents the region of shock wave oscillation. In addition, the range of 55% to 62% of the blade chord length is exactly the separation point oscillation region analyzed above, which indicates that shock wave oscillation directly causes the change of the separation point position of 22 blades in space, and which is bound to affect the blade aeroelastic stability. The main cause of significantly reduced aerodynamic damping of 2ND is the separation of the boundary layer induced by shock waves, which results in upward migration of flow along the blade. As inlet distortion increases, shock wave oscillations on the blade surface become wider and more intense, and the stability of the flow field near the blade surface is affected more.

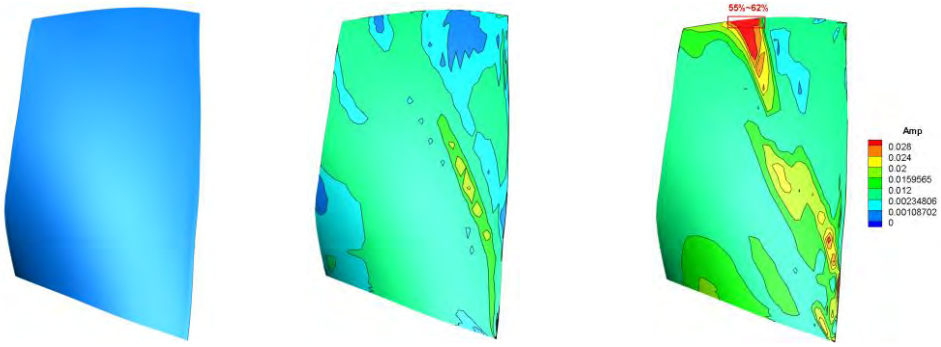

(a) Clean (b) DIS-0.95 (c) DIS-0.9

Figure 14: Amplitude Distribution on the Suction Side in Three Cases

CONCLUSIONS

An in-house coupled CFD/CSD numerical code is used for the prediction of aeromechanical characteristics of the rotor blades with inlet total pressure distortion. The results indicate that:

（1） In terms of aerodynamic characteristics, the presence of inlet distortion reduces the stability margin of the fan, causing the near stall point to get closer to the stall boundary. In the aspect of aeroelastic stability, At DIS-0.9, the aerodynamic damping value of 2ND decreases sharply compared with less than 5% under DIS-0.95. The decrement in aeroelastic stability is non-linear with the increase in distortion coefficient.

（2） The FFT amplitude spectra of the modal displacement indicate that the nND mode exhibits a beating component of nEO. This component is particularly pronounced in odd-order scenarios, attributed to the interaction between the distortion pattern and blade vibration. At "DIS-0.9", the amplitude of the 2EO beating component increases significantly, the oscillation form of the shock wave of a sine function contains obvious second-order excitation, which has nothing to do with whether the inlet distortion has large 2ND amplitude. Which nodal diameter is excited the most depends on the frequency content of the flow, it is the reason why the damping of 2ND is significantly reduced under ”DIS-0.9” distortion conditions.

（3） The boundary layer separation caused by shock waves and the airflow migrating upward along the blade will reduce the aeroelastic stability. As the distortion coefficient increases, the shock wave oscillates along the balde chord

and gradually intensifies. The amplitude distribution of unsteady pressure on the suction side of the blade proves that the axial position change of the separation point caused by shock wave oscillation is the most obvious at DIS-0.9, which significantly reduces the aeroelastic stability.

NOMENCLATURE

$\vec{q}$	Conservative Variable Vector	AIP	Aerodynamic Interface Plane
Ω	Control Volume	BLI	Boundary Layer Ingestion
$\partial\Omega$	Boundary of Control Volume	HCF	High Cycle Fatigue
$\overrightarrow{F_c}$	Convective Fluxes	EO	Engine Order
$\overrightarrow{F_v}$	Viscous Fluxes	RANS	Reynolds-averaged Navier-Stokes
$\vec{S}$	Source Term Vector	HGAE	Hybrid Grid Aeroelasticity Environment
M	Mass Matrix	ALE	Arbitrary-Lagrangian Eulerian
C	Damping Matrix	FVM	Finite Volume Method
K	Stiffness Matrix	MUSCL	Monotone Upstream-centered Scheme for Conservation Laws
Q	Aerodynamic Force Vector	FFT	Fast Fourier Transformation
x	Displacement Vector	ND	Nodal Diameter
q	Generalized Coordinate Vector	IBPA	Inter-Blade Phase Angle
ϕ	Mode Shape Matrix	CFD	Computational Fluid Dynamics
P^*	Total Pressure	CSD	Computational Structural Dynamics

REFERENCES

C. E. Danforth. “Distortion-Induced Vibration in Fan and Compressor Blading.” *Journal of Aircraft*, Vol. 12, No. 4(1975), pp. 216-225.

G. PLOURDE, F. ROBERTS, and F. SMAKULA. “Insights into axial compressor response to distortion.” *4th Propulsion Joint Specialist Conference, Joint Propulsion Conferences*, ()

Gregory Herrick. “Effects of Inlet Distortion on Aeromechanical Stability of a Forward-Swept High-Speed Fan.” *46th AIAA/ASME/SAE/ASEE Joint Propulsion Conference & Exhibit, Joint Propulsion Conferences*, ()

Gregory P. Herrick. “Assessing Fan Flutter Stability in Presence of Inlet Distortion Using One-way and Two-way Coupled Methods.” *50th AIAA/ASME/SAE/ASEE Joint Propulsion Conference, AIAA Propulsion and Energy Forum*, (AIAA 2014-3733)

Greitzer EM. “Surge and Rotating Stall in Axial Flow Compressors—Part I: Theoretical Compression System Model.” *ASME. J. Eng. Power.* 1976;98(2):190-198.

Halliwell D G . Effect of Intake Conditions on Supersonic Unstalled Flutter in Turbofan Engines[J]. Journal of Aircraft, 1980, 17(5):300-304.

Hsuan Yeh. “An Actuator Disc Analysis of Inlet Distortion and Rotating Stall in Axial Flow Turbomachines.” *Journal of the Aerospace Sciences*, Vol. 26, No. 11 (1959), pp. 739-753.

J. ADAMCZYK. “Unsteady fluid dynamic response of an isolated rotor with distorted inflow.” *12th Aerospace Sciences Meeting, Aerospace Sciences Meetings*, ()

Kirsten P. Duffy, Andrew J. Provenza, Milind Bakhle, James B. Min, and Ali Abdul-Aziz. “Laser Displacement Measurements of Fan Blades in Resonance and Flutter During the Boundary Layer Ingesting Inlet and Distortion-Tolerant Fan Test.” *2018 AIAA Aerospace Sciences Meeting, AIAA SciTech Forum*, (AIAA 2018-1892)

Lecht, M., “Investigation of the Behavior of Axial Compressor Stages with Steady Stage Inlet Distortions.” *DFVLR-FB* 83-39, 1983.

Mazzawy RS. “Multiple Segment Parallel Compressor Model for Circumferential Flow Distortion.” *ASME. J. Eng. Power*. 1977;99(2):288-296.

Milind A. Bakhle, Tondapu S. Reddy, Rula Coroneos, James B. Min, Andrew J. Provenza, Kirsten P. Duffy, George L. Stefko, and Gregory Heinlein. “Aeromechanics Analysis of a Distortion-Tolerant Fan with Boundary Layer Ingestion.” *2018 AIAA Aerospace Sciences Meeting, AIAA SciTech Forum*, (AIAA 2018-1891)

Pan T , Yan Z , Lu H ,et al.Forced Response Induced by Low Engine Order Under Circumferential Inlet Distortions With Different Extents[J].Journal of turbomachinery, 2023.

Pearson, H., & McKenzie, A. (1959). “Wakes in Axial Compressors.” *The Journal of the Royal Aeronautical Society*, 63(583), 415-416.

Provenza AJ, Duffy KP, Bakhle MA. “Aeromechanical Response of a Distortion-Tolerant Boundary Layer Ingesting Fan.” *ASME. J. Eng. Gas Turbines Power*. 2018;141(1):011011-011011-10.

Reid, C. “The Response of Axial Flow Compressors to Intake Flow Distortion.” *ASME 1969 Gas Turbine Conference and Products Show* American Society of Mechanical Engineers, 1969:V001T01A029.

Strazisar A J, et al., “Laser anemometer measurements in a transonic axial-flow fan rotor.” NASA TP-2879, 1989.

Yao J, Gorrell SE, Wadia AR. “High-Fidelity Numerical Analysis of Per-Rev-Type Inlet Distortion Transfer in Multistage Fans—Part I: Simulations With Selected Blade Rows.” *ASME. J. Turbomach*. 2010;132(4):041014-041014-10.

ZHENG Y, TIAN X, YANG H. “Impact of blade deflection on the aerodynamic performance of a transonic fan”. *Journal of Aerospace Power*, 2011, 26(7):1621-1627. (in Chinese)

ZHENG Y, YANG H. “Coupled Fluid-structure Flutter Analysis of a Transonic Fan.” *Chinese Journal of Aeronautics*, 2011, 24(3):258-264.

ZHENG Y, YANG H. “Full assembly fluid/structured flutter analysis of a transonic fan.” *Journal of Beijing University of Aeronautics and Astronautics*, 2013,39(5): 626-630. (in Chinese)

ZHENG Y. “Computational aeroelasticity with an unstructured grid method.” *Journal of Aerospace Power*, 2009, 24(9):2069-2077. (in Chinese)